EES Batteries

PAPER

View Article Online
View Journal | View Issue

Cite this: *EES Batteries*, 2025, **1**, 878

Small-scale, long-duration, and biodegradable zinc–air batteries†

Jingwen Zhang * and Mark G. Allen

The Internet of Things (IoT) consists of multiple networked nodes, typically comprising transducers and communication capability, that collect and exchange data to achieve a system goal. As IoT node adoption increases, the impact of e-waste on the environment must be considered. Many IoT nodes are therefore incorporating biodegradable sensors. A recent example is that of precision agricultural systems, in which biodegradable IoT nodes are placed on or below the soil to monitor the plant environment over timescales from weeks to months. Such nodes require energy sources that also biodegrade without harm to the environment. Herein we report Zn–air batteries fabricated from biodegradable materials, and characterize battery performance under sensor-relevant power requirements. The battery comprises a biodegradable Zn anode, a hydrogel electrolyte, and an air cathode (normally consisting of a gas diffusion layer and a catalyst layer). Battery dimensions studied range from 2 × 2 × 0.7 cm^3 (large cell) to 10 × 8 × 5 mm^3 (corn cell, approximately the size of a corn kernel). A scalable biowax encapsulation process was developed for battery passivation. A variety of hydrogel compositions and corrosion inhibitors were investigated to extend battery lifetime. Under discharge, large cell peak power densities ranging from 10 to 50 mW cm^{-2}, and lifetimes ranging from 15 days to 340 days, were achieved. Similarly, corn cell peak power densities ranging from 6.5 to 7.5 mW cm^{-2}, and lifetimes ranging from 7 days to 82 days were achieved. Battery operation was measured both in air and soil environments, showing the potential of this approach for environmental IoT applications.

Received 18th February 2025,
Accepted 9th May 2025

DOI: 10.1039/d5eb00032g

rsc.li/EESBatteries

Broader context

The rapid development of the Internet of Things (IoT) has facilitated data collection, enhanced collaborative decision-making, and enabled system-level solutions to critical applications. The operational efficacy of IoT relies upon the widespread deployment of sensing and actuation nodes and associated power sources. For applications of IoT in natural environments, such as environmental monitoring and precision agriculture, a further constraint is that these power sources must have a benign environmental profile. This study presents the design and characterization of scalable zinc–air batteries constructed from biodegradable materials, aimed at enhancing both the biodegradability and the operational lifespan of IoT sensors and power sources. Natural biowaxes are selected as the packaging material, and a wax encapsulation process is developed to ensure long-term protection during battery operation. Performance characterization is conducted under IoT-relevant discharge conditions, both in the air and buried under soil. By engineering the gel electrolyte and cathode materials, the lifespan of the batteries is extended to a duration of several agricultural seasons. Additionally, the wax-encapsulated zinc–air batteries are miniaturized to the size of a corn kernel to facilitate deployment. The results indicate that wax-encapsulated zinc–air batteries are promising long-term power sources for sustainable IoT applications such as precision agriculture.

Introduction

Recent advances in sensor fabrication, wireless communication, and data analysis have led to the establishment and widespread implementation of IoT. Such IoT networks can be a powerful tool for monitoring large physical areas in a variety of applications, including the natural environment as well as agriculture.[1] The deployment of a variety of subsurface sensors that monitor ambient conditions such as soil moisture, temperature, and nutrient level, enable the collection of accurate information about the field or farm in real time;[2] such information can be used to drive subsequent agricultural optimizations or interventions in the field.

For long-term operation of an IoT network node, whether continuously or intermittently, available energy resources become one of the most crucial challenges. Such sensor networks are often expected to operate without human interven-

Department of Electrical and Systems Engineering, University of Pennsylvania, Philadelphia, PA, USA. E-mail: zjwen@alumni.upenn.edu

† Electronic supplementary information (ESI) available. See DOI: https://doi.org/10.1039/d5eb00032g

tion; however, in many applications, they are expected to be deployed in areas away from convenient access to the established energy grid. Although conventional on-board energy sources could be used to power these sensors, it would be time-consuming and costly to re-collect the nodes or to replace the energy sources once they are depleted. One solution to this problem is developing biodegradable onboard energy sources that can power the sensors during their functional lifetime, and passively degrade in an environmentally benign fashion after use, removing the need for any post-use retrieval.

Batteries (or electrochemical cells; these terms will be used interchangeably here) are an attractive approach to the required energy sources. The material requirements for biodegradable batteries are more stringent than for conventional batteries, considering that not only do the batteries need to exhibit good electrochemical performance and stable output over the operation lifetime, but also have the additional constraint of passive degradation into nontoxic products, especially in agricultural settings.[3] Multiple investigators have begun to research such biodegradable batteries. For example, Esquivel *et al*. reported a degradable primary capillary flow battery using organic redox species, cellulose, carbon, and beeswax.[4] These batteries operated for up to 100 min with an output voltage of 0.5–0.7 V, after being activated with the addition of water. Navarro-Segarra *et al*. presented an evaporation flow redox battery.[5] Liquid biodegradable chemicals stored in reservoirs flow through porous carbon electrodes where the electrochemical reaction takes place, with evaporation as the pumping force. The battery has a working voltage of 0.25–0.75 V under 500–100 μA, and can discharge at 100 μA for up to 4 days. Ko *et al*. reported a biodegradable magnesium alloy–tungsten (AZ31–W) battery, which has a lifetime up to 9.4 days under 50 μA cm^{-2} with about 1 V output voltage.[6]

When considering longer-lifetime application scenarios, air batteries may offer an attractive alternative approach to achieving biodegradable energy sources. A typical metal–air battery comprises a metal anode and an air cathode, separated by an electrolyte and/or a separator,[7] and encapsulated by a package. The metal is oxidized into metal ions at the anode, while oxygen from the ambient air is absorbed and reduced to hydroxide ions in the presence of H_2O at the cathode. In such batteries the oxidant is not stored within the battery volume but instead is extracted from the ambient; this feature not only enables a high energy density of the battery, but also a reduced environmental impact since there is no cathode reactant enclosed.

For the anode, Mg and Zn are the most popular biodegradable metals previously utilized in transient batteries.[3,8] Zn–air batteries are especially promising for long-duration applications, due to their low corrosion rate, coupled with high theoretical specific energy density (1084 W h kg^{-1}), flat discharge voltage, and low cost.[7] Zn will oxidize into ZnO after discharge, which is a bio-safe material and has been used as fertilizer, as it can release Zn^{2+} into the cultivation medium.[9] Zn^{2+} acts as a micronutrient of plants, and most plants contain 30–100 mg Zn kg^{-1} dry matter.[10,11]

For the cathode, commercially available Platinum (Pt)-loaded carbon air cathodes are conventionally used. Although such cathodes often yield high power capability, their high cost could limit IoT applications where many disposable nodes are desired. In low power IoT, carbon cathodes without metal catalysts but with high surface area can be considered.[12]

For the electrolyte, the biodegradable and water-soluble polymer poly-(vinyl alcohol) (PVA) together with conducting ionic species can be formed into a hydrogel; this gel then functions both as the electrolyte host as well as a separator for Zn–air batteries.[13,14]

For passivation, natural waxes are promising and cost-effective materials for biodegradable packaging needs, considering their high hydrophobicity, bio-compatibility, non-toxicity, and abundance in nature.[15,16] Beeswax and soy wax have been investigated as a waterproofing package material for biodegradable batteries and sensors, as well as in slow-release fertilizers.[4,17–19] Beeswax is composed of hydrocarbons, fatty acids, and long-chain esters, while soy wax contains fatty acids and glycerol.[20,21] Both types of wax can be degraded in soil in the presence of moisture, oxygen, and microorganisms (such as bacteria and fungi) through aerobic degradation and metabolic processes, ultimately decomposing into carbon dioxide and water.[22,23] Sui et la reported a maize growth test with these waxes buried in soil, in which, the introduction of waxes in the soil has no obvious detrimental effect on maize biomass growth and development.[18] The package for a battery is expected to be hard and cohesive, therefore resistant to external forces. A comparison of physical properties of biowaxes can be seen in the ESI (Table S1†).

Herein we investigate biodegradable air batteries with Zn anodes, carbon-based cathodes with and without Pt catalysts, hydrogel electrolytes with alkaline or neutral ionic species, and packages of mixtures of natural waxes. The effect of battery size, environment (*i.e.*, in-air or in-soil), and discharge mode (constant or duty cycle) on battery performance and lifetime is assessed.

Materials and methods

Alkaline and neutral PVA-based hydrogel fabrication

PVA-based gel electrolytes with two types of ionic species were fabricated and investigated. The gels were classified based on the pH of the gel after rehydration.

Alkaline gel fabrication. The preparation of PVA–KOH–K_2CO_3 alkaline gel followed the procedure developed in our previous work.[14] Briefly, the PVA–KOH–K_2CO_3 gel electrolyte precursor was made by first heating 10 mL of deionized (DI) water to 85 °C (hotplate set to 140 °C), followed by dissolving 1.5 g of PVA (MW 88 000–98 000, hydrolyzed 90%–percent of the side groups are –OH, Alfa Aesar) in the water while stirring vigorously at 700 rpm. Stirring and heating were maintained for 3 hours. This solution, termed the PVA solution, was then allowed to cool to room temperature (RT). A second alkaline solution was produced by dissolving 1.5 g KOH (potassium

hydroxide, 85%, Sigma Aldrich) and 0.64 g K_2CO_3 (potassium carbonate, >99%, Sigma-Aldrich) in 10 mL DI water; this solution was then added dropwise to the PVA solution at RT. The solution was stirred continuously at 700 rpm for approximately one hour at room temperature to form the uniform alkaline gel precursor. A glass Petri dish was cleaned by IPA and DI water and a controlled amount of precursor (depending on the required thickness of the final gel) was cast on the dish, dried in a desiccator for 8–10 hours, and rehydrated in a rehydration solution prepared by adding K_2CO_3 to a saturated KOH solution in the mass ratio of 1 : 5.3 K_2CO_3/KOH solution. After rehydrating for over 3 days for thorough infiltration, a hollow steel punch with a diameter of 0.5 inch was used to cut the gel and obtain the alkaline gel discs for characterization or battery tests.

Neutral gel fabrication. A PVA solution was prepared as described above. A second near-neutral solution was produced by dissolving 1.9 g NH_4Cl (>99.5%, Sigma Aldrich) in 10 mL DI water. This second solution was added dropwise to the PVA solution at 85 °C, and stirred continuously for approximately one hour at 700 rpm to form the NH_4Cl gel precursor. The precursor was cooled to RT and then cast on a plastic Petri dish. The dish was then placed in a freezer at −25 °C for 24 hours, followed by a one-hour thaw at RT to facilitate physical cross-linking of the precursor. This freeze–thaw process was repeated 4 times to form the neutral gel film as shown in the ESI (Fig. S1†). The gel was stored in the freezer at −25 °C, taken out 1 hour before use to thaw, and punched with the hollow steel punch with a diameter of 0.5 inch to obtain the neutral gel disc.

Battery assembly

Battery active components preparation. For anodes, Zn foils (250 μm in thickness, 99.99% pure, Sigma-Aldrich) were micro-machined using a 532 nm machining laser (IPG IX280-DXF) into a 1 cm diameter circle with a 3 mm wide handle protruding from the circle (later the handle was expanded to 0.8 cm wide).

For air cathodes, platinum-loaded carbon paper (4 mg cm^{-2} Platinum Black – Carbon Paper Electrode, Fuel Cells Store), and different types of carbon papers without metal catalyst (Sigracet 22 BB, Sigracet 29 AA, Toray Carbon Paper 060, and Freudenberg H24C5 Fuel Cells *etc.*) were purchased and cut into 1 cm diameter discs using a hollow steel punch.

Wax package preparation. The wax packages are comprised of a bottom pad and a top pad. The fabrication of wax packages begins with the preparation of molds for the wax as described in the ESI (Fig. S2†). Beeswax (Beesworks Yellow Beeswax Pellets, 100% pure, Cosmetic grade, Amazon) and soy wax (Natural Soy 444 Candle Making Wax, Brand Golden Foods, Amazon) were mixed in a mass ratio of 3 : 1, melted at 80 °C for 4 hours in an oven, thoroughly stirred, and cast in the PDMS mold as shown in Fig. 1(a). The top and bottom pads (20 × 20 × 2 mm^2) were de-molded after solidification at room temperature.

Battery assembly. Batteries were assembled with the wax pads through the encapsulation process depicted in the ESI (Fig. S3†). The three functional layers (anode, hydrogel, and cathode) of the battery were sandwiched between the top and bottom pads, with a thin layer of Ni mesh contacting the cathode side to facilitate testing (this mesh can be replaced by a biodegradable material). Both mesh and anode handle were attached to insulated 34 G Cu lead wires by silver paste for secure external connection. Finally, the four edges of the two pads were manually sealed with melted wax with interconnects enclosed, leaving the Cu lead wires extended through the wax package. In this way, the parasitic leakage current was avoided when the battery was discharged in soil. In addition to the

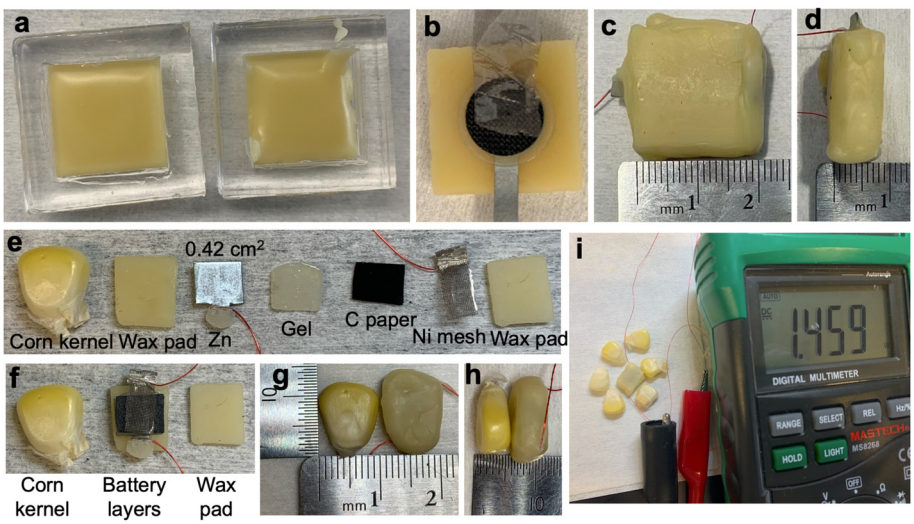

Fig. 1 (a) Top view of melted wax formed within PDMS molds. (b) Top view of battery active layers on a wax pad. (c) Top view and (d) side view of a wax-encapsulated battery. (e) Corn cell components, (f) active layers stacked on a wax pad, (g) and (h) dimension of an assembled corn cell, (i) open circuit voltage of a corn cell.

above sealing process, some batteries were additionally dip coated in wax as described in the ESI.† Fig. 1(b) shows the battery layers stacked on top of a wax pad with the uppermost layer being the cathode contact mesh. Fig. 1(c) and (d) show a wax-encapsulated battery and its dimension.

Reference batteries without wax packaging were also tested using a clamp board technique as described in our previous work.[14]

Loctite sealing for air path verification

To assess potential air paths in the wax package between the internal electrochemical components of the battery and the external environment, a UV-curable instant adhesive (Loctite 4311) was optionally used to reinforce and seal potential parasitic air paths along the Cu wires extending from the inside to the outside of the wax package. A wax-encapsulated battery with the carbon cathode (Sigracet 22 BB,), approximately 200 mg alkaline gel (PVA–KOH–K_2CO_3 gel), Zn anode, and Ni mesh current collector was fabricated. Subsequently, the Loctite adhesive was painted around the egress point of the Cu wires and cured under a UV lamp for 1 min. This process was repeated twice to ensure a tight seal, as shown in Fig. S4 in the ESI.†

Corn cell fabrication

To achieve a battery the size of a seed, each component of the battery was scaled down to the size of a corn kernel as shown in Fig. 1(e) and (f). The footprint of the anode, gel, and cathode was controlled to be 6 × 7 mm^2. After the final dip-coating sealing step as shown in Fig. 4(d), the corn cell was of the dimension 10 × 8 × 5 mm^3 as shown in Fig. 1(g) and (h). Fig. 1(i) shows a corn cell with an OCV of 1.46 V after assembly.

Implementation of corrosion inhibitors in corn cell

Polyethylene glycol 600 (PEG 600, Alfa Aesar), Polysorbate 20 (Tween 20, Sigma Life Science), and Maltodextrin (Maltodextrin powder, 419699, dextrose equivalent 16.5–19.5, Sigma-Aldrich) were purchased and used as received.

Two approaches were taken to incorporate the inhibitors into the battery. One is to mix PEG 600 and Tween 20 in a 1 : 1 mass ratio and paint the mixture onto the Zn anode surface to form the protective layer between the hydrogel and the anode. The second approach is to add the MLD to the gel by dissolving it in the gel precursor and the rehydration solution at a concentration of 0.3 g L^{-1}. To achieve the former, 0.006 g MLD powders was dissolved in the alkaline solution containing 1.5 g KOH and 0.64 g K_2CO_3 (in 10 mL DI water) to form the alkaline gel precursor containing MLD. The rehydration solution was prepared by dissolving 0.011 g MLD in 60 g saturated KOH solution (37.5 mL), then K_2CO_3 was added to the saturated KOH solution with MLD in a mass ratio of 1 : 47.6.

Soil test environment

Batteries were tested in the ambient air and in soil. To characterize in-soil performance, the batteries were placed in organic raised bed soil (Harvest Organics, Lowe's) inside 600 mL beakers at a controlled buried depth of 5 cm. Fig. 2(a) shows the schematic of the battery in-soil test setup. Fig. 2(b) shows a wax-encapsulated battery in a beaker half-filled with soil. After the battery was placed, extra soil was placed on top until the desired depth was reached as shown in Fig. 2(c), and no more water was added to the soil during the battery test. Copper wires extend from the buried battery for external characterization.

Performance characterization

Electrochemical assessment was performed using a BioLogic BCS-805 Ultra-Precision battery cycler. A 10 minute open circuit potential test was first carried out to stabilize the batteries in their respective environments. A current–voltage (*I–V*) curve to demonstrate the power capability of the battery was then performed through a galvanodynamic test with a scan rate of 5 mA s^{-1} from 0 to 100 mA. Battery performance was then characterized by chronopotentiometry testing. Batteries with Pt-loaded cathodes were discharged at 30 μA, which is selected based on the power requirements of typical MEMS fabricated oxygen sensors as well as RFID chips.[24,25]

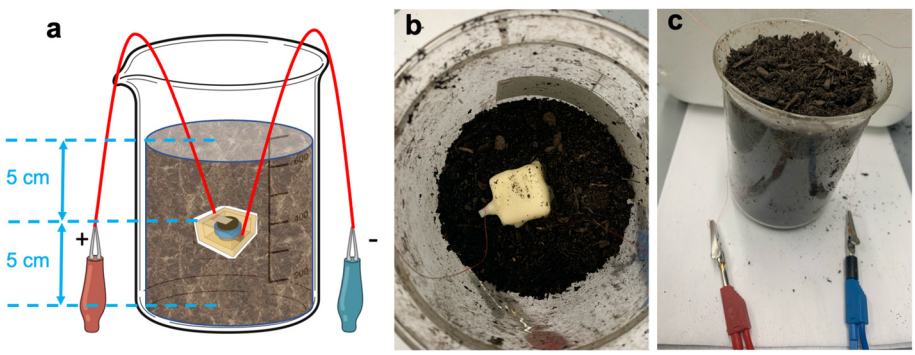

Fig. 2 (a) Schematic of battery soil test setup, (b) top view of a battery prior to adding the top layer of soil, (c) front view of soil-buried battery test set-up.

To verify the air path, batteries with or without the Loctite sealing were tested at a constant current load, which was progressively lowered from 1 mA to 0.015 mA through a multi-step discharge (1–0.030–0.015 mA). For a 1 mA current load, the battery was discharged for 2 h to enable the voltage to reach a plateau value. The battery was then rested for 1 min allowing the OCV to revive. A 30 μA current load was then applied to the battery for 1 h, followed by a 1 min OCV test (current load is 0). Finally, a 15 μA current load was applied to the battery for another hour. A test step will be forced to stop if the voltage falls below 0 V, jumping to the next test step in the queue.

In many cases, sensor nodes in IoT applications do not operate continuously, but instead with a duty cycle, for example, waking up periodically to collect and transmit data.[26,27] In duty-cycling schemes, the node could be switched off to save energy, maximizing its operational lifetime, and also avoiding network congestion.[28] The battery lifetime may depend on the corresponding duty cycle. To measure the battery lifetime in a typical intermittent scenario, batteries were discharged at a 5% duty cycle (discharge at 30 μA for 3 min in a one hour period).

Results and discussion

Table 1 is a summary of the various battery types, geometries, and tests undertaken. Each permutation will be discussed below.

Prior to implementing the testing of Table 1, three studies on battery subcomponents were performed: a package study to understand the air diffusion paths, an alkaline gel study to optimize the gel parameters, and a cathode study to investigate the effect of the presence or absence of Pt in the cathode on the power performance of the battery.

Wax package study

Fig. 3(a) shows the discharge profile of the battery without the Loctite sealing. The output voltage under a discharge current of 1 mA dropped gradually to 0.56 V within 2 hours, implying a relatively low internal oxygen level, as shown in ESI Fig. S5.† The low internal oxygen level was attributed to the relatively high oxygen consumption rate and the low oxygen replenishment rate. When the discharge load changed to 30 μA and

Table 1 Summary of wax-encapsulated batteries tested in this study

Battery	Gel electrolyte	Cathode material	Corrosion inhibitors	Discharge load	Testing environment
Large cell[a]	Alkaline	Carbon paper	—	Continuous 30 μA	In the air
Large cell	Alkaline	Carbon paper	—	Continuous 30 μA	5 cm under soil
Corn cell[b]	Alkaline	Carbon paper	PEG 600 + Tween 20	Continuous 30 μA	In the air
Corn cell	Alkaline	Carbon paper	0.3 g L^{-1} MLD	Continuous 30 μA	In the air
Corn cell	Alkaline	Carbon paper	0.3 g L^{-1} MLD	5% duty cycle	In the air
Corn cell	Alkaline	Carbon paper	0.3 g L^{-1} MLD	5% duty cycle	5 cm under soil
Large cell	Neutral	Pt-Loaded carbon paper	—	5% duty cycle	In the air
Large cell	Neutral	Pt-Loaded carbon paper	—	5% duty cycle	5 cm under soil

[a] Large cell refers to a battery of size 2 × 2 × 0.7 cm^3 after encapsulating in wax, with a Zn anode of 1 cm diameter. [b] Corn cell refers to a battery of size 10 × 8 × 5 mm^3 after encapsulating in corn-sized wax package.

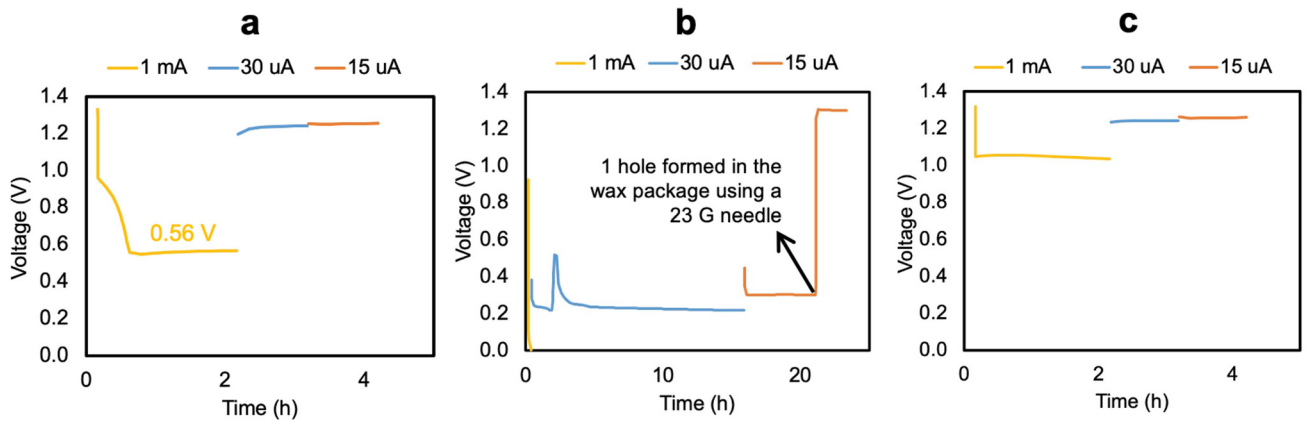

Fig. 3 (a) Discharge curves at step currents 1 mA–30 μA–15 μA for the battery without Loctite sealing, (b) discharge curves at step currents 1 mA–30 μA–15 μA (an extended 16 hours discharge under 0.030 mA current load for oxygen to diffuse in the wax package) for the battery with Loctite sealing, a hole was formed in the wax package with a 23 G needle at approximately 21 h, and (c) discharge curves at step currents 1 mA–30 μA–15 μA of the same battery with Loctite sealing after the hole was formed.

15 μA, the working voltage recovered to 1.2 V, which shows that before the Loctite sealing, the oxygen flux entering the battery was sufficient to support a 30 μA discharge, but not a 1 mA discharge. However, after sealing with the Loctite, the battery was no longer able to output over 1 V voltage even at 15 μA, demonstrating constrained air paths which led to the diminished oxygen flux, as shown in Fig. 3(b). Once a new air path was created by insertion and removal of a 23-gauge needle through the wall of the package, the battery voltage revived quickly as gas replenished the wax package. Fig. 3(c) shows that with this new air path, the battery can output 1 V even at 1 mA.

These results explained the operation of the wax-encapsulated battery without nominal air paths under a 30 μA discharge current. The small gaps formed around the Cu wires are the main air paths of the battery, enabling a sufficient amount of oxygen to access the battery. After blocking the gaps, the flux of air diffusing through the wax encapsulation is insufficient to support a 30 μA discharge. This shows that the wax acts as an oxygen barrier in this package, and that oxygen transport pathways can be designed independently of the diffusion properties of the wax itself.

For the further battery characterization work described below, the air paths along the wires extending from the inside to the outside of the wax package were utilized to provide airflow necessary for a long term discharge current of 30 μA.

Alkaline gel study

An alkaline gel study was undertaken using the large cell format, alkaline gels of various thicknesses, and Pt-loaded carbon cathode. Our previous work showed that the total output energy of the battery will increase with the gel mass when it operates in the gel-limited condition, and that batteries with minimal exposure to the working environment have the longest lifetime.[14,29,30] Wax-encapsulated batteries with increasing amounts of gel electrolyte were assembled and discharged under a constant 30 μA both in the air and soil. Fig. 4(a) shows that an increase in the gel mass from 36 mg to approximately 250 mg resulted in an up to 3.6 times increase in battery lifetime. By increasing the gel electrolyte beyond 300 mg, the battery lifetime did not exhibit significant improvement. The *I–V* curves of these batteries have a similar trend, as shown in Fig. 4(b). Although different masses of gel may result in varying distances between the electrodes and thus a different internal impedance, since batteries are encapsulated within the wax package with constrained air flux, this flux may be the dominant factor that determines the maximum current at which such wax-encapsulated batteries can operate.

Two potential mechanisms behind the observed variation of battery lifetime include carbonation and slow decomposition of an intermediate reaction product.[30] The OH^- ions in the hydrogel provide the ionic conductivity for the battery. While theoretically no OH^- will be consumed in the overall reaction, CO_2 from external sources can diffuse together with O_2 into the battery and react with the OH^- ions in the alkaline electrolyte to form CO_3^{2-} or HCO_3^-, which have much higher ionic resistivity than OH^-.[31] Zn is oxidized and combines with hydroxide ions in the electrolyte, forming soluble zincate ions ($Zn(OH)_4^{2-}$). This process continues until the zincate ions in the electrolyte reach saturation, at which point zincate begins to decompose into zinc oxide and release hydroxide ions.[32] A relatively slow zincate decomposition at early stages of discharge may result in slow hydroxide ion regeneration.[33–36] When the amount of gel electrolyte is relatively small – *e.g.*, the tested 38 mg gel, the OH^- could be consumed gradually over time (as well as the electrolyte pH falling over time) as the battery discharges. When the concentration of OH^- falls too low, the reduced ionic conductivity can induce a large overpotential, leading to the end of discharge.

Gels when encapsulated in the wax package have less than 20% weight loss over 79 days, as shown in Fig. S6 and Table S2 in the ESI.† In ambient air, such gels normally dried out completely within several days. This shows the wax package can provide a good moisture barrier that keeps the gel hydrated for long-term battery operation.

As the battery lifetime increased to over two weeks, cracks in the wax package along the edges were observed as shown in Fig. 4(c). This cracking resulted from the volume expansion of the Zn anode during the electrochemical reaction. This emerging defect during discharge in the package could expose the

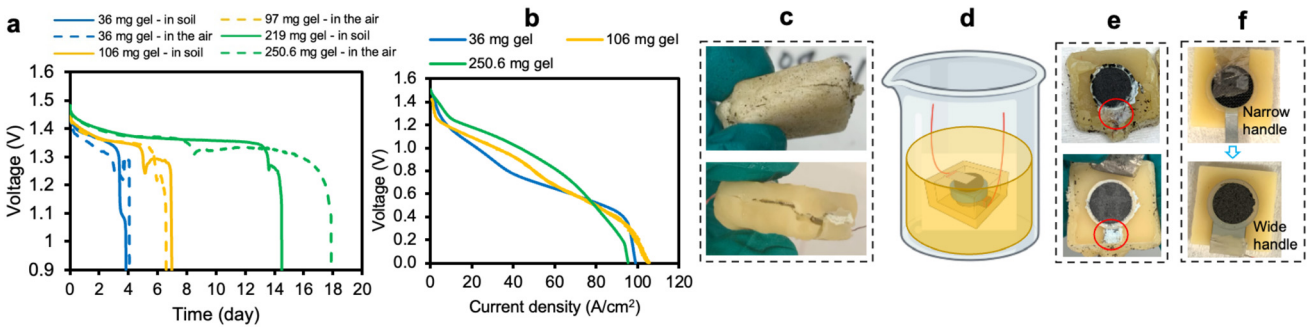

Fig. 4 (a) 30 μA discharge curves and (b) *I–V* curves of wax-encapsulated batteries with different masses of gels in the air and soil. (c) *I–V* wax package cracking of batteries discharged over 2 weeks, (d) additional dip-coating process to enhance the package, (e) consumption of Zn handle, (f) bare narrow handle *versus* wide handle wound with Cu wire, paint-coated by silver paste followed by a dip-coated layer of wax.

Table 2 Carbon-based materials properties

Materials	Thickness/μm	PTFE treatment	Microporous layer	Macroporous layer
Toray 060	190	Yes	No	Yes
Sigracet 29 AA	180	No	No	Yes
Sigracet 22 BB	215	Yes	Yes	Yes
Freudenberg H24C5	270	No	Yes	Yes

internal battery components to the external environment, and the contact between the battery active component layers might loosen due to the lack of stack pressure from the package. Fig. 4(d) shows an additional fabrication step implemented after manually sealing the edges of the wax encapsulation. The entire battery was dip-coated in melted wax as described in the ESI to form an additional conformal layer, thereby improving the mechanical strength of the wax package and preventing cracking.

The batteries after discharge, were disassembled to inspect the condition of the active components. As shown in Fig. 4(e), it was observed that in some cases, the Zn anode handle had turned into ZnO and broken before the main part of the Zn anode (the part facing the cathode) was fully consumed. This could be attributed to the consumption of the handle if exposed to the electrolyte (*e.g.*, if any liquid electrolyte is squeezed out from the hydrogel and wets the handle) and oxygen.[37] To address this issue, a new design of Zn anode with a handle roughly three times as wide was implemented as seen in Fig. 4(f). The wider handle was wound with Cu wire and coated with silver paste at the connection region. Subsequently, the interconnect was dip-coated in melted wax to form an additional hydrophobic protective layer, thus preventing reaction at the handle and maintaining the electrical connection over the long-term test. Due to the success of this anode passivation technique, it was utilized in all subsequent large cell tests.

Carbon cathode study

An investigation into substitute cathode materials was undertaken to reduce the cost and further increase the biodegradability of the battery. The air cathode typically consists of a gas diffusion layer for oxygen transfer (comprising a macroporous layer) and an active catalyst layer (typically microporous), where the oxygen reduction reaction (ORR) occurs.[38] The Pt-loaded cathode used in the above alkaline gel study contains Pt particles in the catalyst layer, with carbon paper serving as the gas diffusion layer. Additionally, hydrophobic material such as poly-tetrafluoroethylene (PTFE) is optionally used to treat the cathode. Noble metal catalyst, However, carbon with high surface area, vacancy defects, and porous structure as activity sites has been reported as an electrocatalyst for the oxygen reduction reaction.[39,40] The indirect two-electron reduction pathway is favored on most of the nanostructured carbons, where oxygen molecules are reduced to the intermediate product H_2O_2.[38] Carbon without a metal catalyst has been found to provide catalytic activity for the oxygen reactions in nonaqueous electrolytes for Li–air batteries, especially at low current density.[12] In this case, carbon functions not only as the catalyst support but also as a good ORR catalyst. To explore the feasibility of Pt-free cathodes, four types of carbon-based materials were tested with the alkaline hydrogel and Zn anode (Table 2). Fig. 5(a) and (b) show the microporous layer structure of the Sigracet 22 BB and Freudenberg H24C5.

Batteries were initially assembled with these carbon-based materials as the cathode (with the micro-porous layer, if present, facing the hydrogel) in the large cell format, using approximately 100 mg gel alkaline electrolyte, and clamp boards to characterize the peak power. Fig. 5(c) and (d) show a comparison of the power curves and *I–V* curves. Batteries with Sigracet 22 BB and Freudenberg H24C5 had a significantly higher peak power and voltage compared to those with Toray 060 and Sigracet 22 AA, potentially attributable to the high surface area of the micro-porous layer. Sigracet 22 BB delivered a higher peak power and voltage than Freudenberg H24C5, due to its highly porous structure in contrast to the flake structure of the Freudenberg H24C5, as shown in Fig. 5(a) and (b). The battery with Sigracet 22 BB carbon cathode was also discharged under higher current loads of 600 μA–8 mA, showing that the carbon cathode alone has sufficient catalytic activity for sensor applications even at higher discharge rates (Fig. S7†).

For all subsequent testing involving non-Pt cathodes (Table 1), Sigracet 22 BB was selected due to its superior power performance. Though the microporous layer of Sigracet 22 BB has been treated with 5 wt% PTFE to make it hydrophobic, the total amount of the PTFE contained in one battery would be less than 0.27 mg (calculated as the PTFE in one cathode 70 g m^{-2} × 0.785 cm^2 × 5 wt%). Alternatively, biodegradable materials could potentially replace PTFE, such as modified hydrophobic nano-scale cellulose fibers or crystals.[41,42]

Wax-encapsulated batteries with carbon cathodes (Table 1, rows 1 and 2)

The above gel and cathode studies were conducted using clamp boards, which have minimal oxygen mass transport limitations. In actual application, both the wax package and soil could significantly limit oxygen transport. To examine this effect, batteries with wax encapsulation were assembled and tested. The peak power of the battery with the wax package in the soil is roughly 1/3 that of the battery with the clamp boards as shown in Fig. 5(e), and the voltage can be lower due to the oxygen diffusion limitation.[14] Although the peak power using this carbon cathode was measured to be 10 mW cm^{-2},

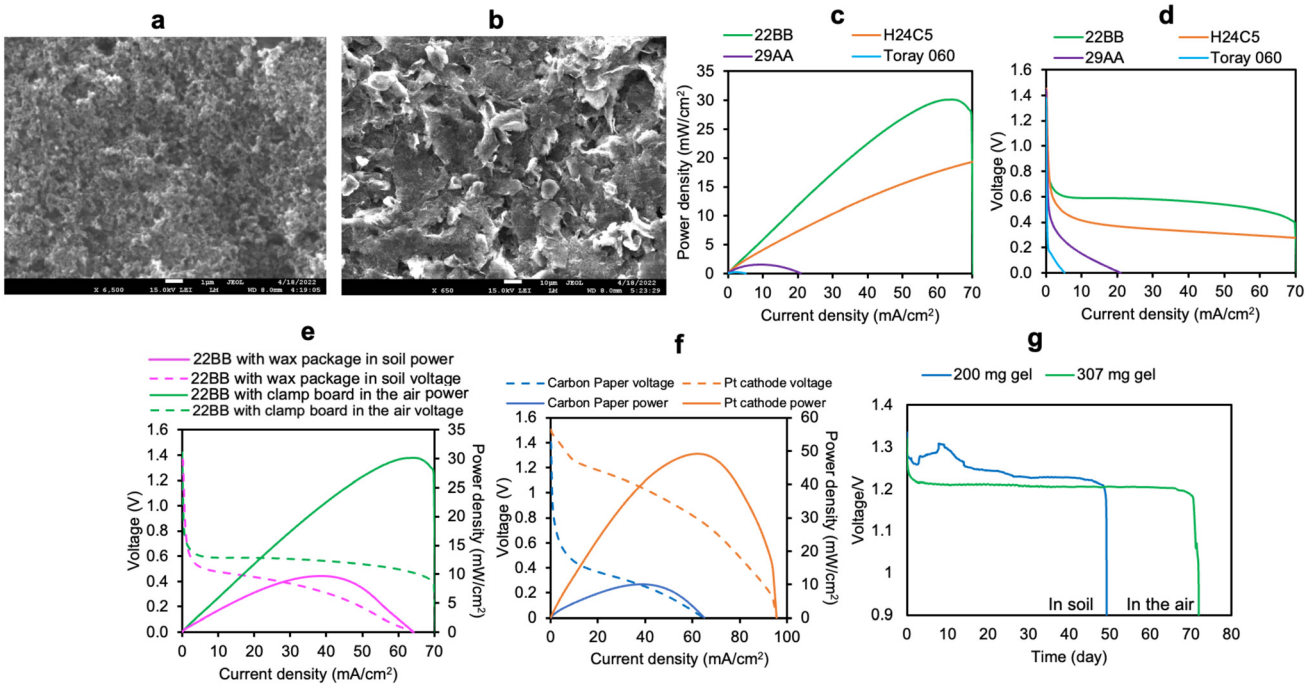

Fig. 5 SEM image of the micro-porous layer of (a) Sigracet 22 BB and (b) Freudenberg H24C5. (c) Power curves and (d) *I*–*V* curves of batteries with carbon-based cathodes assembled by clamp boards. Power curves and *I*–*V* curves of batteries with (e) Sigracet 22BB carbon cathode assembled with clamp boards in the air or wax package in soil, (f) Sigracet 22BB carbon cathode *versus* Pt-loaded cathode with the wax package in soil. (g) Discharge curves of wax-encapsulated batteries with carbon paper cathodes in the soil and the air under 30 μA discharge load.

lower than that of the Pt-loaded cathode as shown in Fig. 5(f), it is still sufficient to fulfill many typical IoT sensor operation requirements of tens of μW. The initial voltage drop in the *I*–*V* curves suggests the activation overpotential difference between the carbon cathode and the Pt-cathode, due to their different catalytic activities.

Furthermore, the battery with the carbon paper cathode discharged for 50 days at the sensor-relevant 30 μA in soil, and a 70 day lifetime was achieved in the air with an increased amount of the gel electrolyte as shown in Fig. 5(g). The relatively shorter lifetime in the soil that is observed may be attributed to the lesser amount of gel electrolyte in the battery, and the environmental effects of the soil. The CO_2 level in soil can be over an order of magnitude higher than that in the air due to microorganism activity.[43] Additionally, the air in soil normally has a much higher relative humidity than atmospheric humidity.[44] Both characteristics of the soil environment can have a detrimental effect on the battery performance. The CO_2 can react with the charge carrier ion OH^- in the gel electrolyte, therefore increasing the internal impedance; the alkaline gel may absorb water when discharged in a high-humidity environment, which can lead to a lower concentration of OH^- and ionic conductivity, and flooding of the porous cathode. However, these effects may be partially mitigated by the low current use case of these batteries, which requires less exposure to the environment because of reduced oxidant flux requirements. The lifetime of these batteries was also found to be longer than the Pt-loaded cathode batteries of the alkaline gel study. These results indicate the utility of carbon cathodes for low-power sensor applications, as well as the potential of Zn–air batteries as biodegradable power sources to sustain long-term operation in subsurface conditions.

Miniaturized batteries (Table 1, rows 3–6)

Battery miniaturization has the potential advantage of utilizing existing agricultural equipment for deployment, therefore shortening the path for adoption of this technology. For example, batteries of the size of seeds could exploit conventional planters for undersoil positioning. To investigate these potential benefits, the battery was miniaturized to the size of a corn kernel, referred to as a "corn cell". Corn cells with alkaline gels and Pt-free carbon cathodes were then fabricated as described above. Fig. 1(i) shows the OCV of the corn cell after assembly was approximately 1.46 V, similar to that of the large cell, demonstrating that the wax encapsulation technology developed can be applied to corn cells.

Power performance study. As the output power of batteries is expected to scale with the battery size, the power performance of corn cells was characterized. Fig. 6(a) and (b) show that batteries of footprint 0.785 cm^2 (large battery format) and 0.42 cm^2 (corn cell format) were assembled with clamp boards. The power density and current density were calculated by dividing the measured power and current by the footprint area. As shown in Fig. 6(c), the corn cell had a similar power density curve to the large battery, implying that the output peak power of the battery would scale down at the scale of the

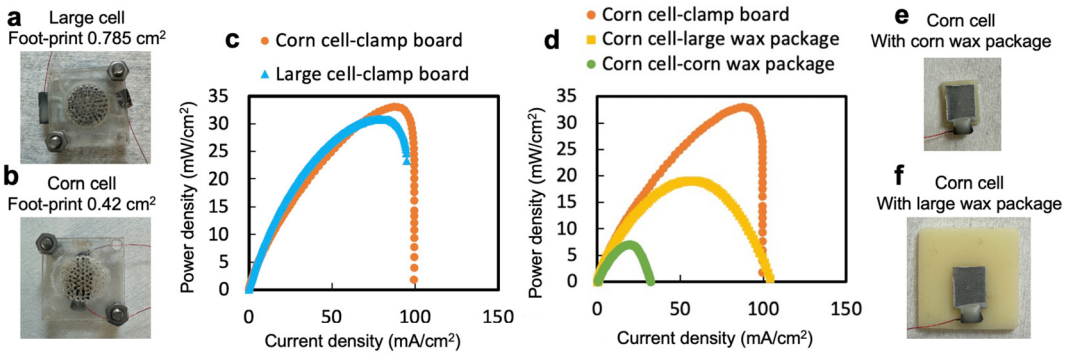

Fig. 6 Top views of (a) a battery with 0.785 cm^2 footprint assembled with clamp boards and (b) a corn cell with 0.42 cm^2 footprint assembled with clamp boards. (c) Power curves of (a) and (b) batteries. (d) Power curves of corn cells with different packages. Corn cell active component layers on top of (e) corn-sized wax pad and (f) large wax pad.

footprint area when no air diffusion barrier of the package is present. Fig. 6(d) demonstrates the effect of the package on the peak power of the corn cell. The peak power density of the corn cell dropped by approximately half when encapsulated within wax pads used for large batteries as shown in Fig. 6(f). As the wax package scaled further down to the size of the corn kernel shown in Fig. 6(e), the peak power density of the corn cell dropped to approximately 7 mW cm^{-2}, potentially due to the reduced amount of air encapsulated, and the slow oxygen replenishment rate. These differences in peak power could be caused by encapsulation reducing air paths or by differences in internal resistance due to different methods of stacking and compressing the cell layers; however, under the typical use case of longer term, low current discharge (*i.e.*, far below the peak power), these differences are expected to be of less concern.

The comparable peak power density of the corn cell and the large cell suggests that their internal impedance normalized by footprint area is similar. The gel mass and anode footprint of the corn cell are approximately 1/4 and 1/2 that of the large cell respectively, while the lifetime of the corn cell (Fig. 7c) is approximately 1/9 that of the large cell (Fig. 5g). Thus, other phenomena that limits the lifetime of the corn cell may be occurring. It should be noted that since the discharge current of both cells was held the same, the discharge current density of the corn cell was double that of the large cell. Additionally, it is possible that the limited internal free space in the corn cell may result in less tolerance to anode expansion caused by ZnO accumulation during discharge and self-corrosion. This hypothesis is also supported by the observation that some corn cells exhibited formation of ZnO along the conducting wire paths, which also could lead to blockage of the parasitic air paths associated with the wires, or even cause damage to the package itself.

Lifetime improvement with corrosion inhibitors. With a constrained amount of anode material, the lifetime of a corn cell could be limited by self-corrosion, especially under a relatively low operational current load. The self-corrosion can also accelerate the anode expansion, which may lead to package failure and air path blockage. Therefore, biodegradable corrosion inhibitors to lengthen the lifetime of the corn cell were investigated. Liang *et al.* introduced a mixture of biodegradable polymer polyethylene glycol 600 (PEG 600) and polysorbate 20 (Tween 20) as composite corrosion inhibitors for Zn/MnO_2 button batteries to suppress the self-discharge of the Zn anode and improve the discharge capacity of the battery.[45] Maltodextrin (MLD) has also been reported to be a biodegradable, inexpensive, and extremely water-soluble inhibitor for Zn corrosion in alkaline and acidic electrolytes.[46,47] These corrosion inhibitors added into the electrolyte would adhere to the Zn surface through adsorption, forming a protective layer that reduces the direct contact of the Zn with the water molecules, therefore reducing the anode self-corrosion rate.

Potentiodynamic polarization tests were performed to quantify the corrosion current and corrosion potential of the Zn anode, using a three-electrode setup shown in Fig. S8.† Fig. 7(a) shows the collected polarization curves for batteries without any corrosion inhibitors, with PEG 600 and Tween 20 on Zn anode, and with hydrogel containing 0.3 g L^{-1} MLD. The corresponding I_{corr} and E_{corr} values are extracted from the polarization curve through Tafel approximation (described in the ESI with Fig. S8†), shown in Table 3. The bare Zn anode has the highest corrosion current of 169 μA, which dropped to 21.6 μA after painting the anode with a thin layer of PEG 600 and Tween 20. The bare Zn anode with a gel containing MLD has a corrosion current of 80.2 μA, higher than the Zn paint coated with PEG 600 and Tween 20, but half that of the battery without inhibitors. The initial efficiency of the corrosion inhibition can be estimated from the reduction in corrosion current of the inhibited group relative to the blank group,[48] which is 87.2% for PEG600 + Tween 20, and 52.5% for Maltodextrin, at the beginning of the discharge.

Based on these electrochemical results, corn cells with corn-sized packages were assembled with Pt-free carbon cathode and alkaline electrolyte, with or without inhibitors to characterize their electrochemical performances. A corn cell with MLD gel has a similar peak power density to the cell with normal alkaline gel, approximately 7.2 mW cm^{-2} as shown in

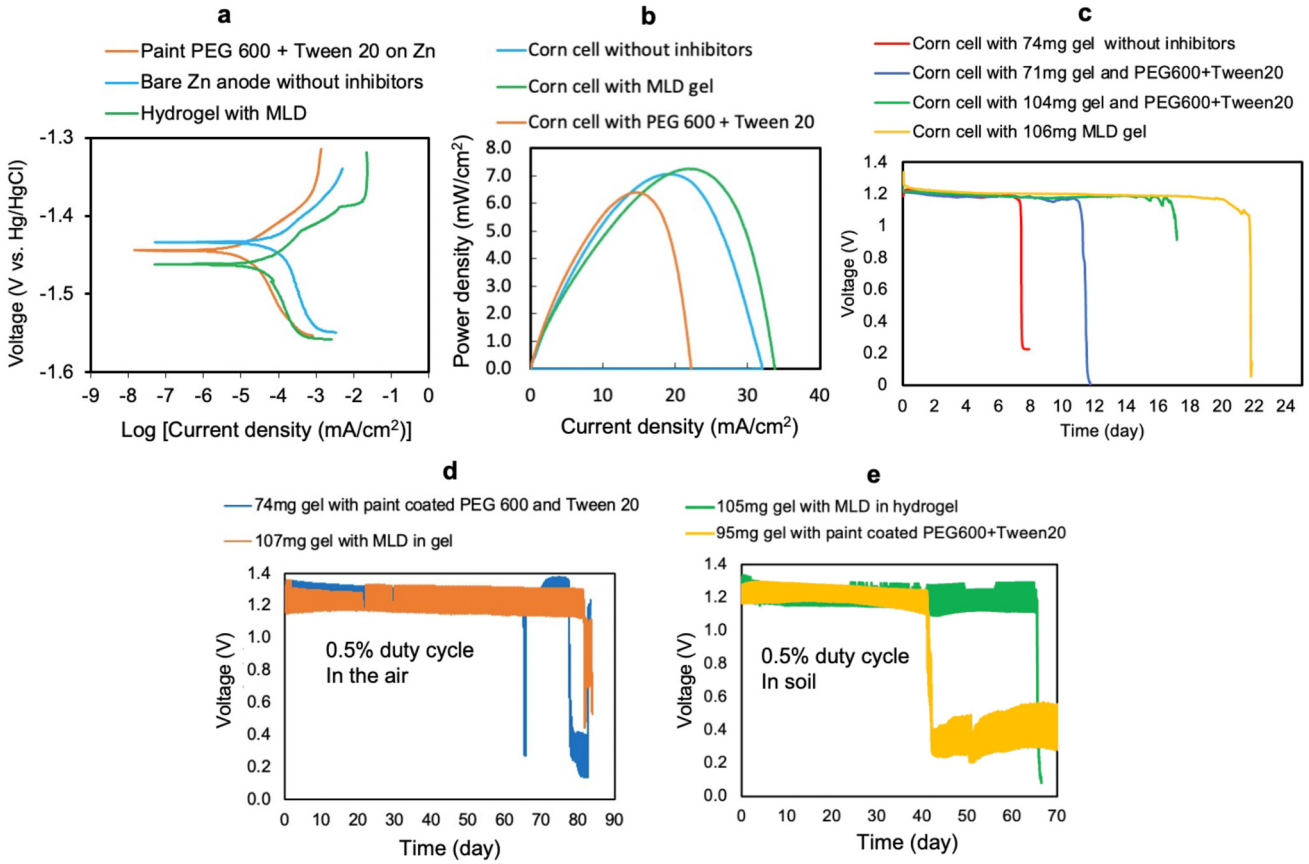

Fig. 7 (a) Polarization curves for batteries without corrosion inhibitors, with PEG 600 and Tween 20 on Zn anode, and with hydrogel containing 0.3 g L^{-1} MLD. (b) Power curves of corn cells without corrosion inhibitors, with PEG 600 and Tween 20 on Zn anode, and with hydrogel containing 0.3 g L^{-1} MLD, (c) discharge curves of corn cells with or without corrosion inhibitors. Corn cell discharge curves with corrosion inhibitors at 5% duty cycle (d) in the air, (e) in soil.

Table 3 Corrosion current and corrosion potential of corn cells without or with corrosion inhibitors

Materials	I_{corr}/μA	E_{corr}/V
Bare Zn	169	−1.43
Zn coated with PEG 600 + Tween 20	21.6	−1.44
Zn with MLD gel	80.2	−1.46

Fig. 7(b). The corn cell with PEG 600 and Tween 20 coated Zn anode has a relatively lower peak power density of approximately 6.4 mW cm^{-2}, potentially due to the polymer film formed at the interface between the anode and the gel. Corn cells were then discharged at 30 μA in the air. Using corrosion inhibitors PEG 600 and Tween 20, together with increased gel electrolyte mass, the lifetime of the corn cell increased from 7.5 days to 17.2 days in the air. In contrast, by introducing MLD into the gel alone, the lifetime of the corn cell was further extended to 21.8 days as shown in Fig. 7(c). The corn cells were also tested under a 5% duty cycle to mimic a typical real-case application scenario. Fig. 7(d) and (e) show that the corn cells with MLD discharged for over 82 days in the air and 65 days in soil, longer than corn cells with PEG 600 and Tween 20 under both conditions. Since the PEG 600 and Tween 20 were initially applied at the anode–gel interface, it is possible that their interfacial concentration could reduce with time, whereas the MLD is stored in the reservoir of gel electrolyte and could replenish the interface and be effective for a longer duration.

Neutral gel batteries (Table 1, rows 7 and 8)

In some applications, the expected operational timeframes for batteries in biodegradable IoT systems can extend over multiple months. For example, in agricultural fields, sensor nodes are expected to be distributed throughout the field during the initial planting process and could be required to operate for the entire growing season to capture complex environmental variables.[49] Therefore, approaches to further extend the battery operational lifetimes are of interest.

It is observed that the alkaline hydrogel of the battery after long-term discharge darkened or disintegrated as shown in the ESI (Fig. S9†). A color change of the alkaline gel from white–yellow to brown to dark brown was noted with time; further, embrittlement of films when stored in high-pH aqueous environments was observed. This discoloration may be attribu-

ted to a deterioration of the chemical structure of the PVA, such as forming polyene fractions, generally caused by oxygen or hydroxyl attack,[50,51] or the formation of a more porous PVA structure due to long-term exposure to a high-pH solution.[52,53] This degradation of the hydrogel may become more severe when the battery is discharged,[54,55] especially over longer durations.

To resolve the degradation issue of the alkaline gel and further extend the lifetime of the battery, a neutral gel electrolyte was investigated. The neutral gel containing NH_4Cl as the ionic species has stable electrochemical properties and high water retention capability.[56,57] Additionally, Zn has a lower self-corrosion rate in the neutral environment.[58,59]

As one potential drawback of batteries with neutral gel electrolytes is the lower power performance compared with alkaline gel electrolytes, a characterization of neutral gel batteries was performed using Pt-loaded cathodes. Power curves of neutral gel batteries were collected in an air environment and were compared to those of the alkaline gel batteries. As shown in Fig. 8(a), a lower peak power of neutral gel batteries was

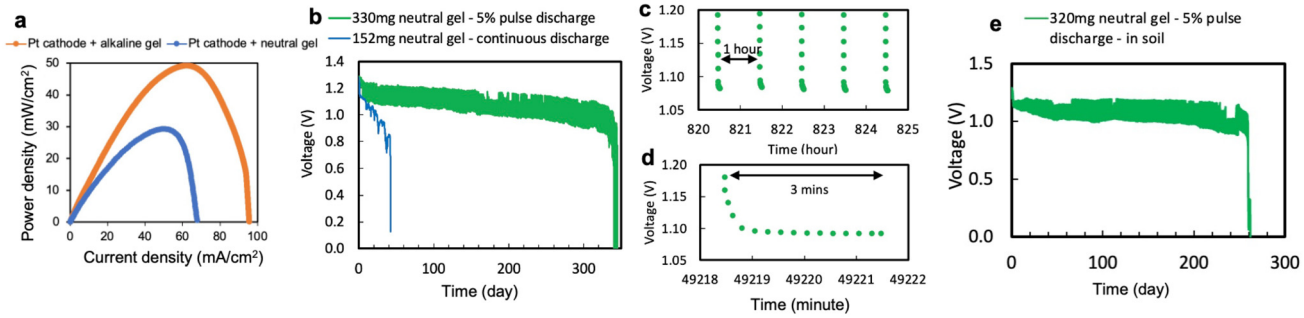

Fig. 8 (a) Power curves of batteries with neutral gel and alkaline gel, when using Pt-loaded cathode. (b) Discharge curves of batteries with neutral gel under 5% pulse and continuous discharge load in the air, (c) zoom-in view of the 5% pulse discharge curve showing the 1 hour period, (d) zoom-in view of the 5% pulse discharge curve showing the battery was discharged for 3 min in an hour. (e) Discharge curve of the battery with neutral gel under 5% pulse in soil.

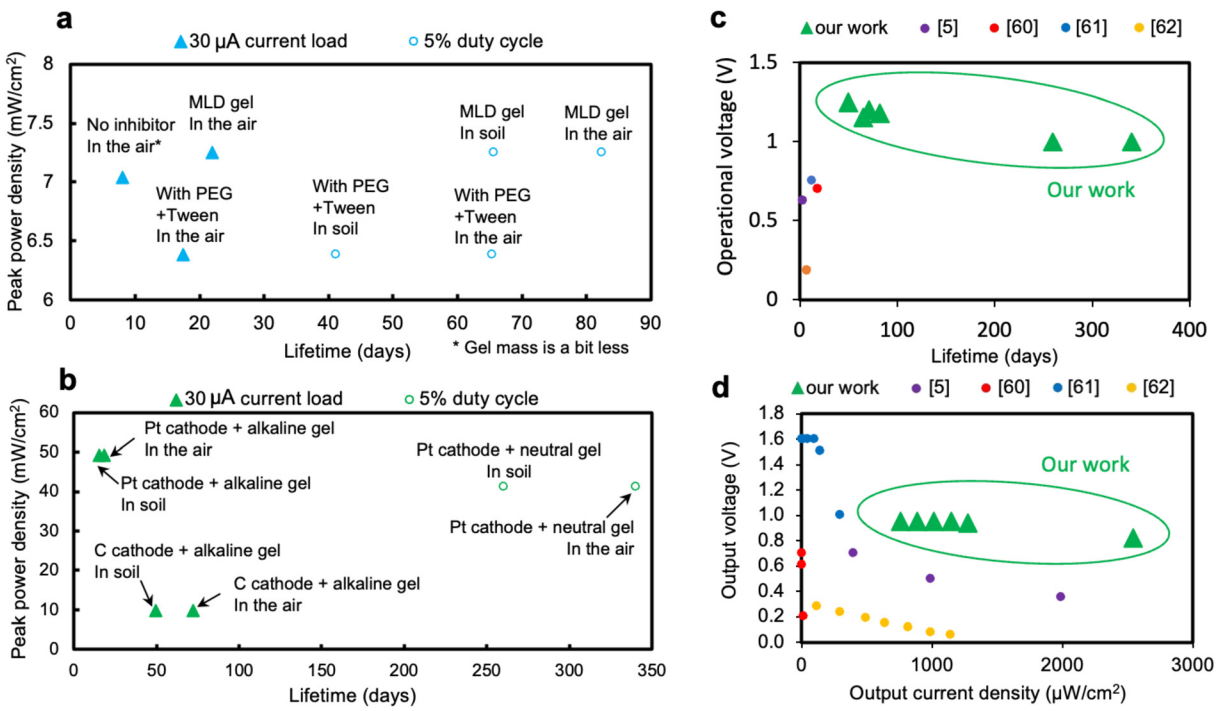

Fig. 9 Summary plots of performances of (a) corn cells and (b) large cells. (c) Long-term operational voltage *vs.* lifetime of various corn and large cells with different electrolytes, corrosion inhibitors, and cathodes (see ESI Table S3† for more detail), and (d) the output voltage under higher current loads of reported biodegradable primary batteries. (* Data of our work in (d) was extracted from the carbon cathode large cell with alkaline gel assembled by clamp boards, see ESI Table S4.†)

observed, potentially due to the lower catalytic activity of the Pt and the higher overpotential of the redox reaction in neutral electrolytes.[57]

Fig. 8(b) shows the discharge curves of neutral gel batteries under continuous 30 μA discharge and under a 5% duty cycle discharge in an air environment. Fig. 8(c) and (d) are zoomed-in views of the 5% duty cycle discharge curve, showing the duty cycle period of 1 hour and the individual 3 minute discharge curve within 1 hour. It was observed that the battery with 330 mg neutral gel has a higher and more stable working voltage under 5% duty cycle discharge. A small degradation in working voltage with time was observed, which may be due to the lower ionic conductivity of the gel as well as the gradual passivation of the Zn anode, since Zn ions have a lower solubility in the neutral environment.[56] Nonetheless, the duty-cycled neutral gel batteries discharged over 340 days in the air environment, and 260 days in soil, as shown in Fig. 8(e). These results demonstrate the potential of a biodegradable neutral gel battery supplying growing-season-long power to an IoT sensor node.

Comparison to the state-of-the-art

Fig. 9(a) and (b) summarize the performance of the various wax-encapsulated batteries studied here. For corn cells, peak power densities range from 6–7.5 mW cm^{-2}, and lifetimes range from 8 days to 82 days. For large format cells, peak power densities range from 10 to 50 mW cm^{-2}, and lifetimes range from 15 days to 340 days.

Fig. 9(c) compares the lifetime and the corresponding operational voltage of batteries discussed in this work to state-of-the-art long-term biodegradable primary batteries reported in the literature.[5,60–62] The wax-encapsulated Zn–air batteries provided stable operational voltage, with lifetimes exceeding the literature-cited batteries by several orders of magnitude. In addition, the Zn–air chemistry compares favorably to literature-cited batteries under high output as shown in Fig. 9(d). These results demonstrate that biodegradable Zn–air batteries may be promising as long-term power sources for environmentally friendly IoT sensor nodes.

Data availability

The data that support the findings of this work are available within the article and the corresponding ESI.†

Conflicts of interest

The authors declare no conflict of interest.

Acknowledgements

This material is based upon work primarily supported by the IoT4Ag Engineering Research Center funded by the National Science Foundation (NSF) under NSF Award Number EEC-1941529. This work was also carried out in part at the Singh Center for Nanotechnology, which is supported by the NSF National Nanotechnology Coordinated Infrastructure Program under grant NNCI-2025608. The authors would also like to acknowledge Dr Yanghang Huang for valuable technical discussion.

References

1 P. Corke, T. Wark, R. Jurdak, W. Hu, P. Valencia and D. Moore, *Proc. IEEE*, 2010, **98**, 903–1917.
2 H. M. Jawad, R. Nordin, S. K. Gharghan, A. M. Jawad and M. Ismail, *Sensors*, 2017, **17**, 1781.
3 N. Mittal, A. Ojanguren, M. Niederberger and E. Lizundia, *Adv. Sci.*, 2021, **8**, 2004814.
4 J. P. Esquivel, P. Alday, O. A. Ibrahim, B. Fernández, E. Kjeang and N. Sabaté, *Adv. Energy Mater.*, 2017, **7**, 1700275.
5 M. Navarro-Segarra, C. Tortosa, C. Ruiz-Díez, D. Desmaële, T. Gea, R. Barrena, N. Sabaté and J. P. Esquivel, *Energy Environ. Sci.*, 2022, **15**, 2900–2915.
6 G. J. Ko, T. M. Jang, D. Shin, H. Kang, S. M. Yang, S. Han, R. Kaveti, C. H. Eom, S. J. Choi, W. B. Han, W. H. Yeo, A. J. Bandodkar, J. Cho and S. W. Hwang, *J. Mater. Chem. A*, 2024, **12**, 32712–32720.
7 J. S. Lee, S. T. Kim, R. Cao, N. S. Choi, M. Liu, K. T. Lee and J. Cho, *Adv. Energy Mater.*, 2011, **1**, 34–50.
8 X. Jia, C. Wang, C. Y. Lee, C. Yu and G. G. Wallace, *MRS Bull.*, 2020, **45**, 121–128.
9 Zinc deficiency in corn, **https://ag.purdue.edu/department/agry/agry-extension/_docs/soil-fertility/zinc-deficiency-in-corn.pdf**, (accessed May 2025).
10 C. Noulas, M. Tziouvalekas and T. Karyotis, *J. Trace Elem. Med. Biol.*, 2018, **49**, 252–260.
11 L. Taiz and E. Zeiger, *Plant Physiology*, Sinauer Associates Inc., Sunderland, 5th edn, 2010.
12 Z. L. Wang, D. Xu, J. J. Xu and X. B. Zhang, *Chem. Soc. Rev.*, 2014, **43**, 7746–7786.
13 V. Venkatesh, Q. Yang, J. Zhang, J. Pikul and M. G. Allen, *2021 21st International Conference on Solid-State Sensors, Actuators and Microsystems (Transducers)*, Orlando, FL, USA, 2021, pp. 1134–1137.
14 J. Zhang, Y. Huang, Q. Yang, V. Venkatesh, M. Synodis, J. H. Pikul, S. A. Bidstrup Allen and M. G. Allen, *ACS Appl. Mater. Interfaces*, 2023, **15**, 6807–6816.
15 F. Wu, M. Misra and A. K. Mohanty, *Prog. Polym. Sci.*, 2021, **117**, 101395.
16 B. Mishra, B. S. Khatkar, M. K. Garg and L. A. Wilson, *J. Food Sci. Technol.*, 2010, **47**, 109–113.
17 Y. Huang, Q. Hu, G. Cui, X. Guo, B. Wei, C. Gan, W. Li, D. Mo, R. Lu and J. Cui, *J. Environ. Sci. Health, Part B*, 2020, **55**, 342–354.
18 Y. Sui, M. Atreya, S. Dahal, A. Gopalakrishnan, R. Khosla and G. L. Whiting, *ACS Sustainable Chem. Eng.*, 2021, **9**, 2486–2495.

19 I. K. Ilic, V. Galli, L. Lamanna, P. Cataldi, L. Pasquale, V. F. Annese, A. Athanassiou and M. Caironi, *Adv. Mater.*, 2023, **35**, 2211400.
20 L. Yao, J. Lio, T. Wang and D. H. Jarboe, *J. Am. Oil Chem. Soc.*, 2013, **90**, 1063–1071.
21 A. P. Tulloch, *Bee World*, 1980, **61**, 47–62.
22 M. Zhu, D. Ying, H. Zhang, X. Xu and C. Chang, *Chem. Eng. J.*, 2022, **446**, 136791.
23 M. Atreya, G. Marinick, C. Baumbauer, K. V. Dikshit, S. Liu, C. Bellerjeau, J. Nielson, S. Khorchidian, A. Palmgren, Y. Sui, R. Bardgett, D. Baumbauer, C. J. Bruns, J. C. Neff, A. C. Arias and G. L. Whiting, *ACS Appl. Electron. Mater.*, 2022, **4**, 4912–4920.
24 SL3S1003_1013 Product data sheet, **https://www.nxp.com/docs/en/data-sheet/SL3S1003_1013.pdf**, (accessed May 2025).
25 D. She and M. G. Allen, *J. Microelectromech. Syst.*, 2019, **28**, 521–531.
26 R. K. Singh, P. P. Puluckul, R. Berkvens and M. Weyn, *Sensors*, 2020, **20**, 4794.
27 J. C. López-Ardao, R. F. Rodríguez-Rubio, A. Suárez-González, M. Rodríguez-Pérez and M. E. Sousa-Vieira, *Sensors*, 2021, **21**, 4281.
28 ETSI EN 300 220-1 V2.4.1 (2012-01), **https://www.etsi.org/deliver/etsi_en/300200_300299/30022001/02.04.01_40/en_30022001v020401o.pdf**, (accessed May 2025).
29 J. Zhang and M. G. Allen, *Solid-State Sensors, Actuators, and Microsystems Workshop*, Hilton Head, South Carolina, USA, 2022, pp. 310–313.
30 Y. Huang, J. Zhang, Q. Yang, V. Venkatesh, J. H. Pikul, M. G. Allen and S. A. B. Allen, *J. Electrochem. Soc.*, 2023, **170**, 100523.
31 G. Li, Y. Wang, J. Pan, J. Han, Q. Liu, X. Li, P. Li, C. Chen, L. Xiao, J. Lu and L. Zhuang, *Int. J. Hydrogen Energy*, 2015, **40**, 6655–6660.
32 T. Otani, T. Yasuda, M. Kunimoto, M. Yanagisawa, Y. Fukunaka and T. Homma, *Electrochim. Acta*, 2019, **305**, 90–100.
33 A. L. Zhu, D. Duch, G. A. Roberts, S. X. X. Li, H. Wang, K. Duch, E. Bae, K. S. Jung, D. Wilkinson and S. A. Kulinich, *ChemElectroChem*, 2015, **2**, 134–142.
34 J. Stamm, A. Varzi, A. Latz and B. Horstmann, *J. Power Sources*, 2017, **360**, 136–149.
35 C. Debiemme-Chouvy and J. Vedel, *J. Electrochem. Soc.*, 1991, **138**, 2538.
36 I. Arise, S. Kawai, Y. Fukunaka and F. R. McLarnon, *J. Electrochem. Soc.*, 2010, **157**, A171.
37 P. Pokorný, M. Kouřil and V. Kučera, *Materials*, 2019, **12**, 1786.
38 J. Pan, Y. Y. Xu, H. Yang, Z. Dong, H. Liu and B. Y. Xia, *Adv. Sci.*, 2018, **5**, 1700691.
39 J. Sun, N. Wang, Z. Qiu, L. Xing and L. Du, *Catalysts*, 2022, **12**, 843.
40 M. A. Alemu, A. A. Assegie, M. Ilbas, R. Al Afif and M. Z. Getie, *Adv. Energy Sustainability Res.*, 2025, 2400414.
41 M. Salajková, L. A. Berglund and Q. Zhou, *J. Mater. Chem.*, 2012, **22**, 19798–19805.
42 Z. Song, H. Xiao and Y. Zhao, *Carbohydr. Polym.*, 2014, **111**, 442–448.
43 M. Maier, V. Gartiser, A. Schengel and V. Lang, *Appl. Sci.*, 2020, **10**, 8653.
44 Soil Air, **https://www.ctahr.hawaii.edu/mauisoil/a_comp04.aspx**, (accessed May 2025).
45 M. Liang, H. Zhou, Q. Huang, S. Hu and W. Li, *J. Appl. Electrochem.*, 2011, **41**, 991–997.
46 M. Pais and P. Rao, *Int. J. Biol. Macromol.*, 2020, **145**, 575–585.
47 M. Pais and P. Rao, *Surf. Eng. Appl. Electrochem.*, 2021, **57**, 374–386.
48 M. N. El-Haddad, *Carbohydr. Polym.*, 2014, **112**, 595–602.
49 C. R. Kagan, D. P. Arnold, M. G. Allen and R. H. Olsson, *2021 IEEE 34th International Conference on Micro Electro Mechanical Systems (MEMS)*, Gainesville, FL, USA, 2021, pp. 350–353.
50 G. Merle, S. S. Hosseiny, M. Wessling and K. Nijmeijer, *J. Membr. Sci.*, 2012, **409–410**, 191–199.
51 G. Merle, M. Wessling and K. Nijmeijer, *J. Membr. Sci.*, 2011, **377**, 1–35.
52 T. N. T. Tran, H. J. Chung and D. G. Ivey, *Electrochim. Acta*, 2019, **327**, 135021.
53 J. Qiao, J. Fu, R. Lin, J. Ma and J. Liu, *Polymer*, 2010, **51**, 4850–4859.
54 Z. Song, J. Ding, B. Liu, Y. Shen, J. Liu, X. Han, Y. Deng, C. Zhong and W. Hu, *Chem. Eng. J.*, 2022, **429**, 132331.
55 Z. Song, X. Liu, J. Ding, J. Liu, X. Han, Y. Deng, C. Zhong and W. Hu, *J. Energy Storage*, 2023, **57**, 106202.
56 K. W. Leong, Y. Wang, M. Ni, W. Pan, S. Luo and D. Y. C. Leung, *Renewable Sustainable Energy Rev.*, 2022, **154**, 111771.
57 C. Wang, J. Li, Z. Zhou, Y. Pan, Z. Yu, Z. Pei, S. Zhao, L. Wei and Y. Chen, *EnergyChem*, 2021, **3**, 100055.
58 C. Lin, S. S. Shinde, X. Li, D. H. Kim, N. Li, Y. Sun, X. Song, H. Zhang, C. H. Lee, S. U. Lee and J. H. Lee, *ChemSusChem*, 2018, **11**, 3215–3224.
59 Z. Zhao, X. Fan, J. Ding, W. Hu, C. Zhong and J. Lu, *ACS Energy Lett.*, 2019, **4**, 2259–2270.
60 X. Huang, H. Hou, B. Yu, J. Bai, Y. Guan, L. Wang, K. Chen, X. Wang, P. Sun, Y. Deng, S. Liu, X. Cai, Y. Wang, J. Peng, X. Sheng, W. Xiong and L. Yin, *ACS Nano*, 2023, **17**, 5727–5739.
61 X. Huang, D. Wang, Z. Yuan, W. Xie, Y. Wu, R. Li, Y. Zhao, D. Luo, L. Cen, B. Chen, H. Wu, H. Xu, X. Sheng, M. Zhang, L. Zhao and L. Yin, *Small*, 2018, **14**, 1800994.
62 P. Nadeau, D. El-Damak, D. Glettig, Y. L. Kong, S. Mo, C. Cleveland, L. Booth, N. Roxhed, R. Langer, A. P. Chandrakasan and G. Traverso, *Nat. Biomed. Eng.*, 2017, **1**, 0022.